ACS OMEGA

Open Access

http://pubs.acs.org/journal/acsodf

Article

Direct Writing of SERS Substrates Using Femtosecond Laser Pulses

Cuiying Huang, Hang Li, and Xinping Zhang*

Cite This: *ACS Omega* 2024, 9, 37188−37196

Read Online

ACCESS | Metrics & More | Article Recommendations | Supporting Information

ABSTRACT: Achieving a high-density, repeatable, and uniform distribution of "hotspots" across the entire surface-enhanced Raman scattering (SERS) substrate is a current challenge in facilitating the efficient preparation of large-area SERS substrates. In this study, we aim to produce homogeneous surface-enhanced Raman scattering (SERS) substrates based on the strong interaction between femtosecond laser pulses and a thin film of colloidal gold nanoparticles (AuNPs). The SERS substrate we obtained consists of irregularly shaped and sharp-edged gold nanoparticle aggregates with specially extruding features; meanwhile, a large number of three-dimensional AuNP stacks are produced. The advantages of such configurations lie in the production of a high density of hotspots, which can significantly improve the SERS performance. When the laser fluence is 5.6 mJ/cm^2, the substrate exhibits the best SERS enhancement effect, and a strong SERS signal can still be observed when testing the concentration of R6G at 10^{-8} mol/L. The enhancement factor of such SERS substrates prepared using femtosecond laser direct writing is increased by 3 orders of magnitude compared to the conventional furnace annealing process. Furthermore, the relative standard deviation for the intensities of the SERS signals was measured to be 5.1% over an area of 50 × 50 μm^2, indicating a highly homogeneous SERS performance and excellent potential for practical applications.

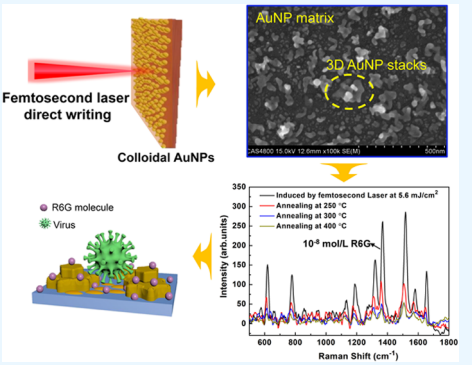

1. INTRODUCTION

Surface-enhanced Raman scattering (SERS) has proven to be an ultrafast, versatile analytical technique with detection limits, which has reached a single molecular weight level and carried fingerprint vibration information on the molecules.[1−6] It has been extensively applied to trace a tiny amount of chemical substances in analytical chemistry,[7,8] biology,[9−12] and environmental science.[13−15] The SERS enhancement mechanisms can be divided into plasmon-induced local electromagnetic field enhancement (EM)[16,17] and charge transfer-induced chemical enhancement (CM).[18−20] The EM enhancement originates from the localized surface plasmon resonance (LSPR) around noble metal nanoparticles induced by incident light. This mechanism significantly amplifies the electromagnetic field, thereby increasing the Raman scattering cross section of nearby molecules. The EM field surrounding a plasmonic nanostructured material is typically nonuniform and tends to be highly concentrated in specific spatial regions known as "SERS hotspots," such as nanotips, interparticle nanogaps (<10 nm),[21,22] or particle−substrate nanogaps. Due to the limited penetration depth of Raman signals and the complex spatial distribution of "hotspots," it is challenging to attain a uniform and reproducible enhancement across the entire substrate.

The techniques for preparing SERS substrates, such as electron beam lithography (EBL) and focused ion beam (FIB), can reach the lowest concentration of 10^{-20} M of rhodamine 6G (R6G).[23] However, these methods require complex processes and expensive equipment, making them unsuitable for industrialized production. Additionally, both EBL and FIB[24] methods are limited in achieving SERS structure preparation on nonplanar substrates, such as microchannels or specific positions of optical fibers. The immersion plating technique is also used for the preparation of SERS substrates due to its simple operation.[25] But immersion plating exhibits shortcomings in precise control of deposition thickness and uniformity, resulting in poor repeatability. It can be applied only to a limited range of metal types. SERS substrates preparation by self-assembly offers a low-cost and simple process;[26,27] the enhancement factor (EF) of silver (Ag) nanoparticles self-assembled in silicon dioxide grooves can reach 10^8.[28] However, there are limitations in material selection for self-assembled templates, inevitable sample contamination, and poor structural controllability. Various self-assembly techniques require precise conditions, including specific solvent compositions, evaporation rates, and particle concentrations. Although Ag exhibits higher SERS sensitivity compared to gold (Au),[29] Au demonstrates strong plasmonic responses in the VIS−NIR range, particularly above 600 nm, which are advantageous, as many biological SERS-based

Received: May 14, 2024
Revised: June 23, 2024
Accepted: August 7, 2024
Published: August 22, 2024

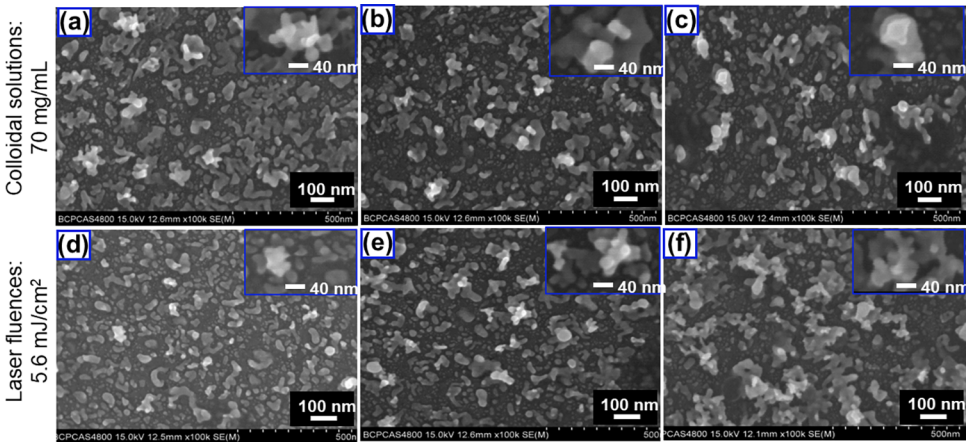

Figure 1. SEM images of AuNP matrix under different concentrations of colloidal solution and laser fluences. SEM images of the AuNP matrix using a concentration of 70 mg/mL of the colloidal solution and laser fluences of 4.4 mJ/cm^2 (a), 5.6 mJ/cm^2 (b), and 6.8 mJ/cm^2 (c). SEM images of the AuNP matrix at a laser fluence of 5.6 mJ/cm^2 using concentrations of the colloidal solution of 50 mg/mL (d), 70 mg/mL (e), and 100 mg/mL (f). Insets are the enlarged SEM images of the 3D AuNP stacks in panels (a)−(f).

detectors use VIS−NIR lasers. In the long term, Au is chemically more stable and biocompatible with many molecules of interest; therefore, Au is the preferred material for SERS substrates in biological and biomedical applications.[30] Compared to the above methods, femtosecond laser direct writing (FLDW) technology offers advantages, such as three-dimensional (3D) processing capability, maskless fabrication, and suitability for nonplanar substrates.[31] Due to the extremely high peak power of femtosecond lasers, which can reach the terawatt (TW, 10^{12} W) level, this technology is versatile in processing a wide range of materials, including metals, for example, Au, Ag,[32,33] Cu,[34] and semiconductors.[35] Compared to traditional two-dimensional (2D) SERS structures, a 3D SERS active platform can extend the interaction area and ensure the ability to directly detect trace amounts of molecules.[36−39] Therefore, developing an efficient method based on FLDW technology to manufacture a homogeneous 3D SERS platform has significant prospects.

The solution-processable fabrication technique, involving colloidal Au nanoparticles (AuNPs), has emerged as an important method for producing both periodic and random-distributed nanostructures.[40,41] This technique offers advantages such as simplicity, large-area fabrication, and flexible tunability in the spectroscopic response of the final structures. However, it generally requires annealing processes, and only in a narrow range of annealing temperatures can it produce densely packed nanoparticles. This makes it difficult to precisely control the preparation conditions and distinctly reduces the reproducibility of the fabrication technique. In addition, whether using a muffle furnace or continuous laser annealing[42,43] results in rounded edges of the nanostructures and makes it difficult to stack into a 3D nanostructure.

Based on the solution-processable method, we utilized the FLDW technique to fabricate SERS substrates with Au nanostructures. In this experiment, colloidal AuNPs were spin-coated onto indium−tin oxide (ITO) substrates, followed by the direct writing of a high-energy femtosecond laser. By the transient thermal effect generated during the interaction between femtosecond laser pulses and colloidal AuNPs, a random AuNP matrix was achieved. This structure consists of irregularly shaped and sharp-edged Au nanoparticle aggregates, which have a high density of hotspots. Additionally, there are numerous 3D AuNP stacks, significantly enhancing the SERS performance of the substrate. The EF is as high as 10^6, with a relative standard deviation (RSD) as small as 5.1% in the selected area on the "mapping" image. This method not only exhibits the cost-effectiveness and capacity for large-scale fabrication but also offers the distinct advantages of negating the need for annealing and demonstrating versatile transferability.

2. RESULTS AND DISCUSSION

2.1. FLDW of Colloidal AuNPs. 1-Hexanethiol-modified AuNPs with mean diameters smaller than 10 nm were synthesized as previously reported.[44] We dissolved the powder of ligand-covered AuNPs into xylene to obtain the colloidal solution with a concentration of 70 mg/mL. Then, we spin-coated the colloidal AuNPs onto a glass substrate deposited with 200 nm thick indium−tin oxide (ITO), which is used to help facilitate the scanning electron microscopy (SEM) measurement. Figure S1 shows an SEM image of the colloidal film sample of AuNPs prior to exposure to femtosecond laser pulses. At this stage, the AuNPs were smaller than 10 nm and coated with a layer of nonconductive sulfur-containing organic ligand, which hindered their observation under the scanning electron microscope. Then, femtosecond laser pulses at a wavelength of 800 nm were used as the pump in a subsequent FLDW process. These 800 nm laser pulses, which have a maximum pulse energy of 1 mJ, a pulse length of roughly 150 fs, and a repetition rate of 1 kHz, were focused onto the surface of the sample with an area of about 12.56 mm^2. The interaction between the femtosecond laser pulses and the colloidal film of AuNPs resulted in a transient thermal effect. This effect caused the sublimation of sulfur-containing organic complexes from the surface of the AuNPs. Subsequently, the AuNPs underwent melting and aggregating, leading to the formation of an AuNP matrix, which was distributed randomly and increased in dimensions. The morphologies of these AuNP matrices exhibited a strong correlation with the laser fluences (Figure 1a−c).

The laser fluence of 4.4 mJ/cm^2 approached the melting threshold of the AuNPs, leading to the observation of some sheet unseparated structures in the substrate, as shown in Figure 1a. Using ImageJ software, we determined that the area

https://doi.org/10.1021/acsomega.4c04588
ACS Omega 2024, 9, 37188−37196

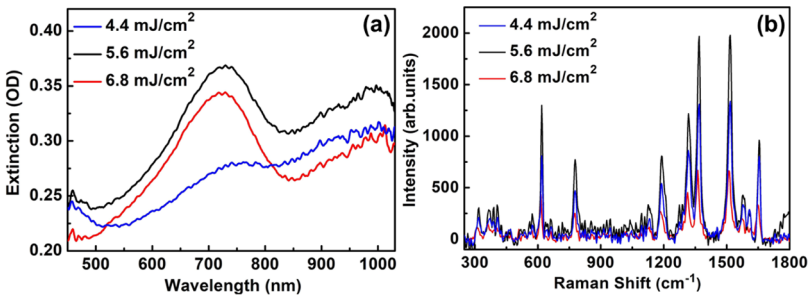

Figure 2. (a) Optical extinction spectra and (b) SERS spectra with 633 nm excitation of the 10^{-6} mol/L R6G modified AuNP matrixes of the SERS substrates obtained at various laser fluences.

fraction of the single-layer AuNP matrix was 42.8%. Furthermore, the particle size distribution of the AuNPs was analyzed based on Feret diameter, revealing that 60.4% of particles were below 25 nm, 33.0% were between 25−100 nm, and 6.6% were above 100 nm (Figure S2). In Figure 1c, larger AuNPs were generated as the laser fluence increased to 6.8 mJ/cm^2, resulting in proportions of particle sizes below 25 nm, between 25−100 nm, and above 100 nm of 55.1, 39.6, and 5.3%, respectively (Figure S2). Simultaneously, the area fraction of the AuNP matrix decreased to 36.4%. This indicates that higher fluence laser pulses not only increased the size of AuNPs but also led to larger separations between them. Figure 1c illustrates that the majority of the AuNPs have gaps exceeding 20 nm.

Thus, it can be seen that the changes in the sizes and gap widths were not completely independent of each other. The laser fluence directly affected the melting and aggregation of the AuNPs. Under lower pulse energy, the AuNPs cannot fully melt, and only a small portion of them melt and aggregate to form Au nanostructures. Conversely, with higher energy pulses, the AuNPs could fully melt and rapidly aggregate at multiple points, forming Au nanostructures with larger sizes and gaps. This poses a challenge when aiming to attain structures with large sizes and small gap widths for enhancing the hotspot density on SERS substrates. In addition, if the energy was excessively high, such as 6.8 mJ/cm^2, it could cause rapid and intense heating of AuNPs. In this case, small-sized particles that did not have sufficient time to aggregate might be vaporized directly. The blank areas observed in Figure 1c were due to the direct vaporization of small AuNPs. This is one of the factors leading to the observed decrease in the area fraction of the AuNP matrix in Figure 1c. In our study, when a laser fluence was 5.6 mJ/cm^2, the proportions of particle sizes below 25 nm, between 25−100 nm, and above 100 nm were 56.7, 35.9, and 7.4%, respectively (Figure S2). Additionally, the area fraction of the AuNP matrix was measured at 45.6%. As is observed in Figure 1b, the AuNP matrix exhibits larger sizes and relatively smaller interspacing.

Two characteristics of the AuNP matrix through the FLDW method were observed in Figure 1a−c. First, we obtained Au nanostructures mainly consisting of irregularly shaped and sharp-edged AuNP aggregates with specially extruding features. This contrasts with the smooth-edged, uniformly sized Au or Ag nanostructures, which can be achieved through muffle furnace annealing,[45,46] thermal evaporation deposition,[47] and interference lithography.[48] Second, as demonstrated in the insets of Figure 1a−c, some AuNPs with various sizes and shapes stacked together and formed 3D stacks. The gap widths between each AuNP of 3D stacks were extremely narrow. The presence of sharp protruding structures and minute gap widths greatly facilitates the formation of SERS hotspots. Moreover, according to the SEM images (Figure 1a−c), the space between these 3D AuNP stacks ranges from 50 to 200 nm, with small AuNPs densely distributed in the space. This structure, as a SERS substrate, can facilitate full contact with analytes of varying sizes. In certain studies, the formed 3D nanostructures are densely distributed.[29] When used as a SERS substrate, such densely arranged 3D aggregates may make it difficult for large analytes (e.g., viruses) to fully embed into the hotspots of the structures. Furthermore, we utilize FLDW, specifically one-step ablation, to obtain 3D AuNP stacks without the need for templates such as TiO_2 nanopores or silica nanospheres in other reports.[28,49] This approach avoids the interference introduced by templates in spectroscopic or SERS detection.

In this experiment, the AuNP (ranging in size from 5 to 10 nm) colloidal film was irradiated with femtosecond laser pulses. Initially, femtosecond laser pulses evaporated the organic substances on the film's surface. Then, due to the strong optical electric fields, the AuNPs underwent rapid melting and agglomeration with their neighboring particles into larger-sized nanostructures. However, the length of the pulse interval (1 ms) is much greater than the pulse length of the femtosecond laser (150 fs), leading to weak thermal accumulation and rapid cooling of the system. This resulted in the process of melting and reaggregation of AuNPs not being able to proceed fully, and solidification occurred again. In addition, the melting points of the particles increased with their size. The following radiation could melt only small-sized AuNPs, and it did not work for particles that had already aggregated in big size. Thus, as shown in Figure 1, the resulting structure emerged as a cluster-like matrix formed by the random aggregates of small AuNPs. It is worth noting that the femtosecond laser pulses acted from the upper layers of the film and penetrated deeper progressively. It was easier to form a 3D aggregate composed of stacked AuNPs in the vertical direction, as can be seen in the insets of Figure 1.

To further optimize the preparation parameters, we compared the differences in the SEM images of the fabrication results with varying concentrations of the colloidal solution (Figure 1d−f). The laser fluence was fixed at 5.6 mJ/cm^2 while the concentration of the colloidal solution was increased from 50 to 100 mg/mL. At a low concentration of 50 mg/mL, the amount of Au nanoparticles is not sufficient to produce 3D AuNP stacks. However, at a high concentration of 100 mg/mL, a large amount of AuNPs and the increased viscosity of the colloidal solution may increase the difficulty of removing residual organic materials on the substrate. Additionally, a large

https://doi.org/10.1021/acsomega.4c04588
ACS Omega 2024, 9, 37188−37196

number of interconnected Au nanoislands were produced. Comparing Figure 1d−f, we find that a concentration of 70 mg/mL is close to optimal.

2.2. Performance of the SERS Substrates Consisting of an AuNP Matrix. *2.2.1. Optical Spectroscopic Performance of the AuNP Matrix Fabricated by FLDW.* Figure 2a shows the optical extinction spectra of the AuNP matrix fabricated by the FLDW technique with different laser fluences, corresponding to those demonstrated in Figure 1a−c, respectively. As commonly observed, AuNPs of smaller sizes show a weaker and narrower localized surface plasmon resonance (LSPR) spectrum at shorter wavelengths. As the size of the AuNPs increases, the resonance spectrum shifts toward longer (red) wavelengths, becoming stronger and broader. Moreover, AuNPs that are more uniform in size exhibit a narrower LSPR spectrum.[43] When the laser fluence is 4.4 mJ/cm^2, the extinction spectrum exhibits a low intensity and broad line width. As shown in the blue curve in Figure 2a, a peak with an intensity of 0.28 OD is observed around 730 nm, while the extinction signals are distributed over the range of 500−1000 nm. This can be attributed to the formation of AuNPs with a small average size (60.4% of particle size below 25 nm, Figure S2) and a broad range of their size distribution under low-energy conditions, as illustrated in SEM image (Figure 1a).

As the laser fluences increase to 5.6 and 6.8 mJ/cm^2, much enhanced optical extinction spectra are observed. These two spectra exhibit relatively narrower bandwidths, both peaking at around 725 nm, with amplitudes of 0.37 and 0.34 OD, respectively. This indicates that with the increase in laser fluence, more uniform-sized AuNPs can be formed. When the femtosecond laser fluence is 4.4, 5.6, and 6.8 mJ/cm^2, we calculated that the area fraction of the single-layer AuNP matrix is 42.8, 45.6, and 36.4%, respectively, and the relative proportion of AuNPs with a Fermi diameter larger than 25 nm is 39.6, 43.3, and 44.9% (Figure S2). Therefore, the primary factor contributing to the enhanced plasmon resonance response around 725 nm (Figure 2a) as the laser fluence increases is the increased size of the AuNPs. Additionally, the intensity of the plasmon resonance response is also influenced by the changes in the gap of the AuNPs. Compared with 4.6 and 6.8 mJ/cm^2, the optical extinction spectra intensity of 5.6 mJ/cm^2 reaches the maximum (the black curve in Figure 2a). This is because the obtained AuNP matrix has larger sizes and smaller separation distances, resulting in a stronger plasmon resonance response under these conditions. It should be noted that an obvious surface plasmonic absorption band is presented around 980 nm in all spectra shown in Figure 2a. Almost all of the AuNPs observed in Figure 1a−c are smaller than 150 nm (Figure S2), and as investigated in our former work,[40] their plasmon resonance spectra have a peak wavelength of less than 650 nm. Therefore, the extinction spectra with peak wavelengths beyond 730 nm are based on the enhanced interfacial plasmonic interactions,[17,42] which can only be observed when the gap width between the structures is very small (typically <10 nm). Two primary mechanisms have been proposed to explain the interfacial plasmons: (1) strong plasmonic coupling between adjacent AuNPs due to the extremely narrow gap widths between them and (2) plasmonic resonance from the collective 3D AuNP stacks rather than isolated AuNP. These mechanisms are the dominant factors responsible for achieving a larger enhancement in SERS performance. It can be observed that the interfacial plasmon signal reaches its maximum intensity when the laser fluence is 5.6 mJ/cm^2 (Figure 2a), resulting in the highest density of hotspots in the SERS substrate.

2.2.2. SERS Performance of the AuNP Matrix Fabricated by FLDW. To evaluate the SERS efficacy of the AuNP matrix fabricated by femtosecond laser irradiation, Raman experiments were conducted employing R6G as the model molecule, owing to its well-established vibrational features. A 20 μL R6G solution in ethanol with a concentration of 10^{-6} mol/L was first dropped on the substrates. SERS measurements were carried out after the complete evaporation of ethanol. It is clear to note that the AuNP matrix fabricated by three different laser fluence yielded high SERS activity, and the Raman spectra show the intense peaks of R6G's main vibrational features of carbon skeleton stretching modes at 618, 778, 1189, 1317, 1368, 1517, 1577, and 1654 cm^{-1}, as shown in Figure 2b.

The global EFs were calculated following the procedures reported in ref 50. According to the definition of analytical enhancement factor EF $= \frac{I_{SERS}/C_{SERS}}{I_{RS}/C_{RS}}$, we choose the SERS peak of 10^{-1} mol/L R6G modified blank ITO−glass substrate as the reference in Figure S3 in the Supporting Information. The EFs at 1517 cm^{-1} were calculated to be as large as 6.2×10^4, 9.2×10^4, and 3.1×10^4 for samples induced by laser fluence of 4.4, 5.6, and 6.8 mJ/cm^2, respectively. The maximum SERS enhancement was observed for the substrate fabricated by a laser fluence of 5.6 mJ/cm^2. This result is consistent with the findings from the previous section, which were based on the analysis of the extinction spectroscopy.

Although the gap widths between the AuNPs are smaller at lower laser fluence, they mostly form unseparated Au nanostructures and are small in size. If we were to use higher laser fluence, then the sizes and separation distances of the AuNPs would increase simultaneously, which would result in a deterioration of the Raman enhancement effect. In fact, larger AuNPs may induce stronger localized fields compared to smaller ones, but the narrow gap widths between them play a more important role due to the further local-field enhancement. Moreover, the AuNP matrix produced with the laser fluence of 4.4 mJ/cm^2 shows relatively stronger interfacial plasmons, as presented by the blue curve in Figure 2a. All of the above explains why the substrate induced by a laser fluence of 4.4 mJ/cm^2 exhibits preferable SERS performance, as opposed to those induced by 6.8 mJ/cm^2 (Figure 2b).

To further verify the concentration of the colloidal solution on the SERS performance of the substrate, we provided the SERS spectra of substrates at different concentrations of the colloidal solution, as shown in Figure S4. SERS measurements were performed on R6G prepared by a solution with a concentration of 10^{-6} mol/L. The EFs at 1517 cm^{-1} were calculated to be 2.0, 6.3, and 2.4×10^4 for samples prepared with the concentrations of 50, 70, and 100 mg/mL, respectively. The maximum SERS enhancement was observed with a concentration of 70 mg/mL colloidal solution. This result is consistent with the findings from SEM image analysis in the previous section, indicating that the concentration of 70 mg/mL is optimal.

2.3. Comparison with the Conventional Annealing Process. Based on the solution-processable technique, Au nanostructures can be fabricated through heating plates or muffle furnaces. These methods enable the preparation of large-area and highly sensitive SERS substrates. To clarify the differences between the conventional annealing process and

https://doi.org/10.1021/acsomega.4c04588
ACS Omega 2024, 9, 37188−37196

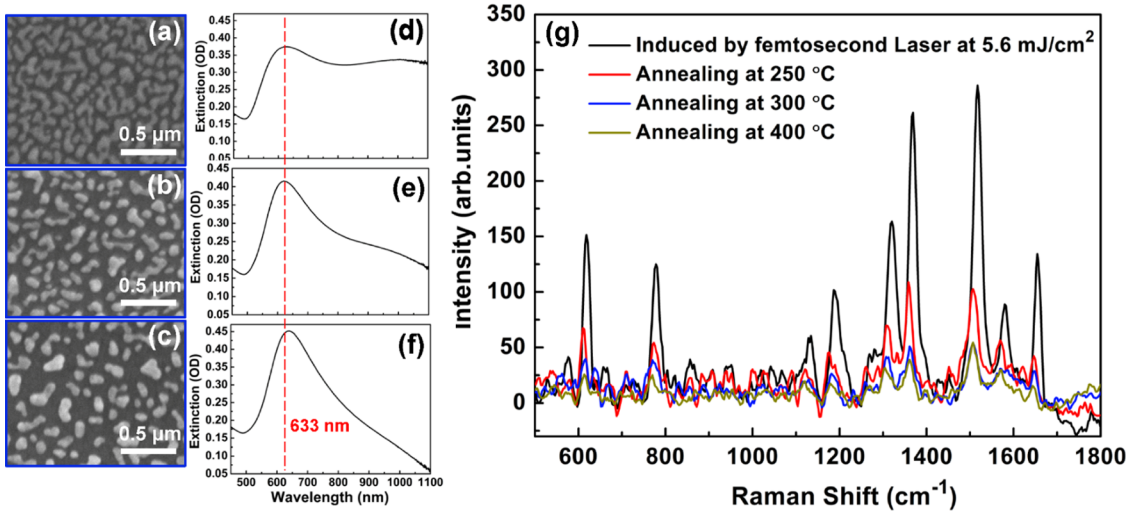

Figure 3. (a–f) SEM images (left panel) and optical extinction spectra (right panel) of samples annealed at temperatures of 250 °C (a, d), 300 °C (b, e), and 400 °C (c, f). (g) SERS spectra with 633 nm excitation using the FLDW technique at a laser fluence of 5.6 mJ/cm^2 for a 10^{-8} mol/L R6G solution (black curve) and SERS spectra from samples annealed at temperatures of 250 °C (red curve), 300 °C (blue curve), and 400 °C (brown curve) for a 10^{-6} mol/L R6G solution.

FLDW technology, we conducted the following comparative experiments. 100 mg/mL colloidal AuNPs were spin-coated on the same ITO–glass substrate and then annealed in a muffle furnace at three temperatures (250, 300, and 400 °C), resulting in the formation of Au nanoisland structures with different sizes and width gaps. According to the SEM images shown in Figure 3a–c, the sizes and width gaps of Au nanoislands increase with annealing temperature. Some interconnected Au nanoislands are obtained at an annealing temperature of 250 °C (Figure 3a). As the temperature increases, the interconnected Au nanoislands separate into isolated ones (Figure 3b,c), which exhibit regular and smooth shapes such as circles and ellipses. And no 3D stacking of AuNPs can be observed in Figure 3a–c. The area fractions of monolayer Au nanoisland structures obtained at annealing temperatures of 250, 300, and 400 °C were 51.0, 42.2, and 30.7%, respectively. Additionally, it was observed that the annealed Au nanoislands were predominantly distributed in the range 75–200 nm, based on Feret diameter analysis of the Au nanoislands (Figure S5).

Figure 3d–f presents the optical extinction spectra of samples corresponding to the SEM images shown in Figure 3a–c, respectively. We observe that the plasmonic response of all three structures peaked at about 633 nm. With an annealing temperature of 250 °C, the peak of spectra is still observed at longer wavelengths (800–1000 nm), as shown in Figure 3d. This phenomenon can be attributed to the formation of structures with narrower width gaps at a lower temperature, leading to the formation of plasmonic dimers or higher-order aggregations. As the temperature increases, the gap widths among the Au nanoislands increase notably, resulting in weak interfacial plasmonic signals. Consequently, no significant plasmon signal is observed in the wavelength range of 800–1000 nm when the annealing temperature increases to 300 or 400 °C (Figure 3e,f). It is noteworthy that the extinction coefficient of the substrate annealed at 400 °C reaches a peak of 0.45 OD at 640 nm (Figure 3f), whereas the extinction coefficient of the substrate obtained by the FLDW technique does not exceed 0.4 OD (Figure 2a). The difference arises because the average size of Au nanoislands obtained through annealing is larger than that of AuNPs prepared by FLDW, as evidenced by a comparison between Figures S2 and S5.

We still chose the 633 nm excitation laser, which is nearly at the peak of the optical extinction spectra, as shown by the red dotted line in Figure 3d–f. The SERS measurements were conducted following the procedure described in Section 2.2.2. It was found that the Raman signals of the 10^{-6} mol/L R6G solution were weak when tested by using the SERS substrates prepared through the conventional annealing process (Figure 3g). This indicates that the samples prepared by furnace annealing have an ultralow detectable concentration of 10^{-6} mol/L. At an annealing temperature of 300 °C (the blue curve in Figure 3g) or 400 °C (the brown curve in Figure 3g), the Raman signals of R6G are hardly observed. When the annealing temperature is 250 °C (the red curve in Figure 3g), weak Raman signals can still be detected at 618, 778, 1317, 1368, and 1517 cm^{-1}, indicating that the sample prepared under lower temperature conditions exhibits a larger improvement of the SERS performance compared with higher temperature conditions. However, when the annealing temperature is below 250 °C, the residual organic compounds on the substrate cannot be removed, which can affect the testing of SERS signals. Nevertheless, we detect a strong Raman signal from a 10^{-8} mol/L R6G solution using the SERS substrate, which was fabricated by FLDW with a femtosecond laser fluence of 5.6 mJ/cm^2 (the black curve in Figure 3g), and the maximum EF at 1517 cm^{-1} can be calculated as 1.3×10^6. Excitation at 633 nm is not located at the spectrum of strongest localized surface plasmons, which is 725 nm, as shown by the black curve in Figure 2a. This implies a possibly much lower detection limit than the observed value of 10^{-8} mol/L. Thus, compared to traditional annealing techniques, the sensitivity of the SERS substrate induced by a femtosecond laser is increased by at least 3 orders of magnitude.

The traditional furnace annealing process is based on the average thermal effect of the metal particles, where the AuNPs are molten and have a chance to "flow" on a "hot" substrate over a "long range." Due to the sufficient freedom of melting and the influence of surface tension, regular structures such as circular or elliptical shapes are formed, as shown in Figure 3a–

https://doi.org/10.1021/acsomega.4c04588
ACS Omega 2024, 9, 37188–37196

c. Furthermore, the substrates do not appear as any 3D AuNP stacks. With the FLDW process, they tend to form AuNPs with sharp morphologies and narrow gap widths. At the same time, a large number of 3D AuNP stacks can be observed. These structures obtained through the FLDW technique have the following advantages for improving SERS performance. (1) The sharp protrusions of the irregular AuNPs and the tiny gap widths between the 3D AuNP aggregates can significantly increase the density of hotspots in the SERS substrate. (2) The 3D AuNP stacks result in an enlargement of the effective contact area between the probe molecules and the SERS substrates, leading to further improvement in the SERS properties. In Figure 4, we present a concept of two different SERS substrates for detecting analytes with various sizes. The substrate prepared by FLDW features 3D AuNP stacks, significantly increasing the surface area of the substrate compared with conventional SERS substrates (here, the annealed Au nanoisland structures). The increased surface area of the substrate can effectively enhance the contact area between the hotspots and R6G molecules, thereby amplifying the Raman signals. For larger-sized analytes, exemplified by viruses in Figure 4, the size of viruses is usually several tens to hundreds of nanometers, and they are composed of complex components such as proteins, DNA, RNA, etc. Due to geometric constraints, most whole viruses cannot fit into the SERS hotspots of conventional SERS substrates (see Figure 4a). However, in the FLDW-prepared substrate, larger viruses can be embedded within the 3D AuNP stacks (see Figure 4b), increasing the portion of the virus surface area that can penetrate into the substrate hotspots, resulting in more comprehensive virus Raman peaks.

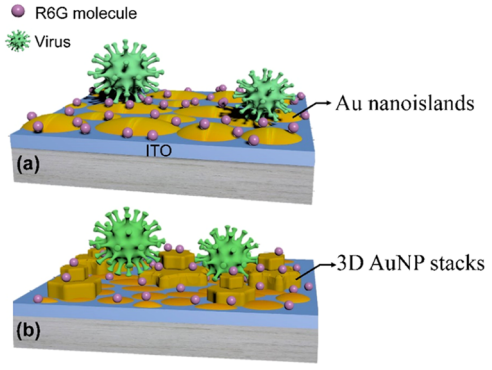

Figure 4. Concept of SERS substrates prepared by (a) furnace annealing and (b) FLDW for detecting R6G molecules and viruses.

In addition, it is important to emphasize that the FLDW process offers several significant advantages over furnace or hot-plate annealing, including the convenient and precise control of the laser power, action time, and scanning area. In contrast, achieving precise control over temperature and the rising−holding−falling time is challenging with furnace or hot-plate annealing methods. Consequently, the FLDW technique facilitates excellent reproducibility of the AuNP structures. Furthermore, the FLDW process typically does not require a high-temperature treatment. This can avoid issues caused by thermal expansion and stress in the materials, making them more suitable for heat-sensitive materials.

2.4. Large-Area Homogeneity. To confirm the homogeneity of SERS enhancement for the AuNP matrix, Raman mappings of the main vibration of R6G were obtained. A 10^{-6} mol/L R6G solution and the substrate prepared by a laser fluence of 5.6 mJ/cm^2 were used in this experiment. The intensity of the Raman vibrational signal at 1368 cm^{-1} on an area of 50 × 50 μm^2 was plotted in Figure 5a. A total of 6400 spectra were obtained in the mapping image. The mappings show different color contrasts from dark to bright red, reflecting the diversity of the SERS enhancement. The main

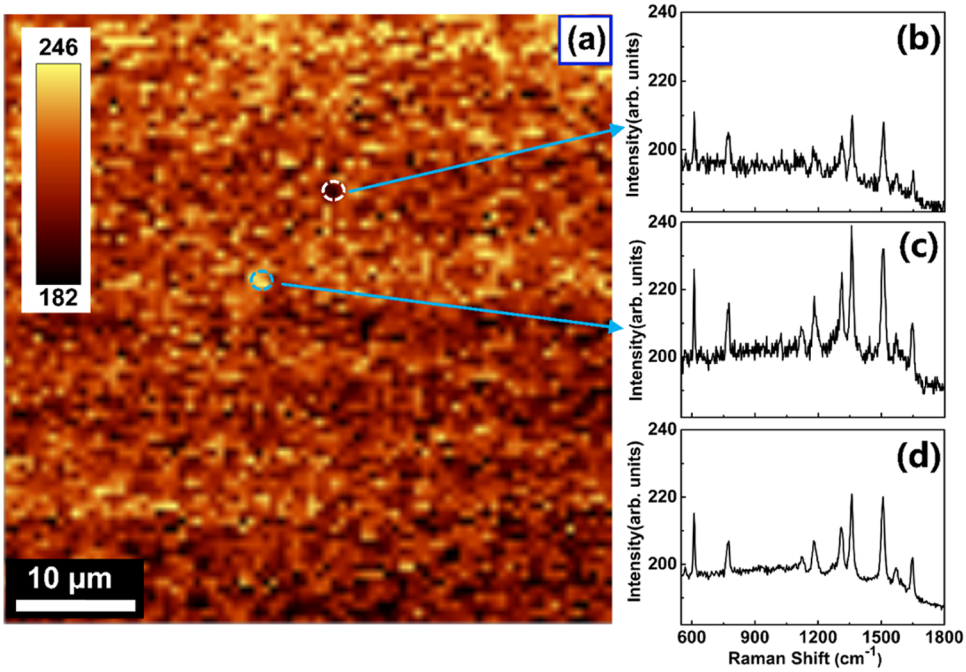

Figure 5. (Left panel) (a) The mapping image on an area of 50 × 50 μm^2 for the Raman vibration at 1368 cm^{-1} of an R6G on SERS sample induced by laser fluence of 5.6 mJ/cm^2. (Right panel) Average SERS spectra on dark (b) and bright (c) spots, which are marked by dotted circles in image (a), and the average SERS spectrum over the entire mapping area (d).

https://doi.org/10.1021/acsomega.4c04588
ACS Omega 2024, 9, 37188−37196

Raman vibrations of R6G were enhanced at all spots, with high contrast and clear boundaries, as shown in Figure 5a. Figure 5b,c shows the SERS spectra on dark and bright spots, which are marked by dotted circles in Figure 5a, respectively. And the average spectrum over the entire mapping area is shown in Figure 5d. The amplitudes of the SERS signal at 1368 cm^{-1} for the dark spot, bright spot, and average spectrum are 210, 240, and 220 (arbitrary units), respectively. The differences among these three values are minimal. The relative standard deviation (RSD) of the Raman intensity, calculated with more than 50 spectra, was 5.1% for Raman vibrations at 1368 cm^{-1}. RSD 5.1% is lower than the acceptable standard of 20%.[51] These results show the uniformity of SERS activity over the entire substrate area.

3. CONCLUSIONS

We present an approach that combines solution-processable techniques with the FLDW process to fabricate SERS substrates, exhibiting large-area homogeneity in a highly reproducible manner. This substrate offers convenience, environmental friendliness, and simplicity in manufacturing operations. It exhibits high sensitivity when using R6G molecules as a probe, with excellent Raman signals obtained even at a concentration as low as 10^{-8} mol/L. This sensitivity is 3 orders of magnitude higher than that achieved through traditional annealing methods. The preparation technology possesses the following advantageous features. (1) Facilitated production of Au nanostructures with irregular, sharp shapes and 3D stacks, which significantly enhance the performance of SERS substrates. This mechanism plays a crucial role in increasing the analytical performance of SERS-based sensors in various applications, including chemical and biological sensing, as well as in trace analysis. (2) Spectroscopy tests have revealed resonance characteristics in the near-infrared spectral region, allowing these metal nanostructures to be applied in other photovoltaic, light-emitting, and photodetection devices. (3) This annealing-free nanofabrication method can be readily applied to fiber tips, soft substrates, and other plasmonic devices for practical optoelectronic and sensing applications.

4. MATERIALS AND METHODS

4.1. Synthesis of Colloidal AuNPs. 1.5 g of tetraoctylammonium bromide and 80 mL of toluene were measured and successively added to a flask. The mixture was stirred slowly until the tetraoctylammonium bromide was completely dissolved in the toluene. Then, 0.32 g of chloroauric acid ($HAuCl_4{\cdot}4H_2O$) was added, and the mixture was stirred for 20 min. 0.36 g of hexanethiol was added to the stirring mixed solution using a pipette. Subsequently, a solution of $NaBH_4$ (0.28 g) dissolved in 20 mL of deionized water was added to the reaction mixture at a uniform rate. The mixture was continuously stirred for 4 h. Then, the mixed solution was poured into a separating funnel and allowed to stand. The subnatant was discarded, and the process was repeated by adding deionized water 3−4 times. The toluene solvent was removed using a rotary evaporator. 20 mL of methanol was added to the obtained product, and residual impurities were further removed through ultrasonication and centrifugation, repeating 3−4 times. The supernatant was removed, leaving the precipitate adhered to the container wall. After drying the resulting product, powdered AuNPs were obtained.

4.2. Fabrication Techniques. The indium−tin oxide (ITO) glass substrates with an area of 15 × 15 mm^2 were cleaned with ethanol and deionized water before being dried. We dissolved the powder of ligand-covered AuNPs into xylene to obtain the colloidal solution. Then, the ITO surface was spin-coated with colloidal AuNPs using a speed of 1800 rpm and a duration of 30 s. For laser direct writing, a Ti:sapphire femtosecond pulse laser amplifier produced by Coherent was used as the laser source. The femtosecond pulse laser was focused onto the surface of the AuNP colloidal film sample after passing through a shutter, attenuator, and lens. The relative position between the sample and the lens was adjusted to ensure that the diameter of the spot on the sample surface was about 4 mm, corresponding to an area of about 12.56 mm^2. The laser beam had powers of 550, 700, and 850 mW, which were focused onto the surface of the sample, resulting in laser fluences of approximately 4.4, 5.6, and 6.8 mJ/cm^2, respectively. The exposure time was 20 min. In this optical setup, the shutter and attenuator could be used to control the time and intensity of the femtosecond laser acting on the sample. For the conventional annealing process, the ITO surface was spin-coated with colloidal AuNPs with a concentration of 100 mg/mL at a speed of 2000 rpm and a duration of 30 s. Then, the samples were sent to the Muffel furnace and heated at three temperatures (250, 300, and 400 °C) for 10 min, respectively.

4.3. Microscopic Characterization. The SEM images of the samples were captured using a S4800 scanning electron microscope from Hitachi.

4.4. Spectroscopic Characterization. The optical extinction/absorption spectra were measured by using a USB4000 spectrometer from Ocean Optics, where a halogen lamp supplied the illumination light source. The optical extinction/absorption spectrum was calculated by $-\log_{10}\frac{I_S(\lambda)}{I_0(\lambda)}$, where $I_S(\lambda)$ and $I_0(\lambda)$ are the transmission spectra through the sample and the ITO substrate, respectively.

4.5. SERS Measurements. The solution sample was initially prepared by dissolving R6G in ethanol at concentrations of 10^{-6} or 10^{-8} mol/L. Subsequently, a 20 μL aliquot of the R6G solution was deposited onto the surface of the fabricated SERS substrate. Upon complete evaporation of the solvent, SERS measurements were conducted using a WITEC Alpha 300A-Confocal Raman imaging system equipped with 633 nm excitation lasers. The effective power of the excitation laser was about 30 mW. A 50× objective (numerical aperture NA = 0.85) was used for all of the measurements, with an integration time of 10 s. In the Raman mapping, we utilized an excitation laser with 633 nm and a power of 0.5 mW to consecutively scan 80 × 80 points within a 50 × 50 μm^2 area. The integration time for each point was 0.5 s. A total of 6400 spectra were collected.

■ ASSOCIATED CONTENT

Data Availability Statement

All of the data are included in the paper.

Supporting Information

The Supporting Information is available free of charge at https://pubs.acs.org/doi/10.1021/acsomega.4c04588.

SEM image of the colloidal film sample of AuNPs prior to exposure to femtosecond laser pulses (Figure S1), the statistic evaluation of the AuNPs Feret diameter

https://doi.org/10.1021/acsomega.4c04588
ACS Omega 2024, 9, 37188−37196

obtained at different laser fluences (Figure S2), SERS spectra with 633 nm excitation of the 10^{-1} mol/L R6G modified blank ITO−glass substrate (Figure S3), SERS spectra with 633 nm excitation of the 10^{-6} mol/L R6G modified AuNP matrix of the SERS substrates obtained at different concentrations of the colloidal solution (Figure S4), and the statistical evaluation of the AuNPs Feret diameter obtained at different annealing temperatures (Figure S5) (PDF)

AUTHOR INFORMATION

Corresponding Author

Xinping Zhang − *Institute of Information Photonics Technology, Beijing University of Technology, Beijing 100124, China;* orcid.org/0000-0001-6534-0004; Email: zhangxinping@bjut.edu.cn

Authors

Cuiying Huang − *School of Arts and Sciences, Fujian Medical University, Fuzhou, Fujian 350122, China; Institute of Information Photonics Technology, Beijing University of Technology, Beijing 100124, China;* orcid.org/0009-0002-1663-3913

Hang Li − *Institute of Information Photonics Technology, Beijing University of Technology, Beijing 100124, China*

Complete contact information is available at: https://pubs.acs.org/10.1021/acsomega.4c04588

Author Contributions

X.Z. and C.H. conceived and designed the research, conducted experiments, analyzed data, wrote the manuscript, and read and approved the manuscript. H.L. helped with the Raman testing.

Notes

The authors declare no competing financial interest.

ACKNOWLEDGMENTS

The authors acknowledge the support by the National Natural Science Foundation of P. R. China (12104092) and the Fujian Medical University Talent Startup Fund (XRCZX2019032).

REFERENCES

(1) Nie, S. M.; Emory, S. R. Probing single molecules and single nanoparticles by surface-enhanced Raman scattering. *Science* **1997**, *275*, 1102−1106.

(2) Pérez-Jiménez, A. I.; Lyu, D.; Lu, Z.; Liu, G.; Ren, B. Surface-enhanced Raman spectroscopy: Benefits, trade-offs and future developments. *Chem. Sci.* **2020**, *11*, 4563−4577.

(3) Wang, T.; Lu, Y.; Xu, L.; Chen, Z. J. Π-conjugated poly(3-hexylthiophene-2,5-diyl) thin film as a SERS substrate for molecule detection application. *J. Mater. Sci.* **2022**, *57*, 16965−16973.

(4) Wu, Z. J.; Sha, M.; Ji, D. Y.; Zhao, H. P.; Li, L. Q.; Lei, Y. Ordered anodic aluminum oxide-based nanostructures for surface-enhanced Raman scattering: a review. *ACS Appl. Nano Mater.* **2024**, *7*, 11−31.

(5) Xu, Y.; Zhong, H.; Shi, M.; Zheng, Z.; Liu, S.; Shou, Q.; Li, H.; Yang, G.; Li, Z.; Xing, X. Microfiber-directed reversible assembly of Au nanoparticles for SERS detection of pollutants. *Opt. Lett.* **2022**, *47*, 2028−2031.

(6) Liu, Y.; Qiao, S.; Fang, C.; He, Y.; Sun, H.; Liu, J.; Ma, Y. A highly sensitive LITES sensor based on a multi-pass cell with dense spot pattern and a novel quartz tuning fork with low frequency. *Opto-Electron. Adv.* **2024**, *7*, No. 230230.

(7) Lai, H.; Li, G.; Xu, F.; Zhang, Z. Metal-organic frameworks: Opportunities and challenges for surface-enhanced Raman scattering - a review. *J. Mater. Chem. C* **2020**, *8*, 2952−2963.

(8) Xu, S.; Man, B.; Jiang, S.; Wang, J.; Wei, J.; Xu, S.; Liu, H.; Gao, S.; Liu, H.; Li, Z.; Li, H.; Qiu, H. Graphene/Cu nanoparticle hybrids fabricated by chemical vapor deposition as surface-enhanced Raman scattering substrate for label-free detection of adenosine. *ACS Appl. Mater. Interfaces* **2015**, *7*, 10977−10987.

(9) Wu, C.; Wang, S.; Luo, X.; Yuan, R.; Yang, X. Adenosine triphosphate responsive metal-organic frameworks equipped with a DNA structure lock for construction of a ratiometric SERS biosensor. *Chem. Commun.* **2020**, *56*, 1413−1416.

(10) Liu, G.; Wei, J.; Li, X.; Tian, M.; Wang, Z.; Shen, C.; Sun, W.; Li, C.; Li, X.; Lv, E.; Tian, S.; Wang, J.; Xu, S.; Zhao, B. Near-infrared-responded high sensitivity nanoprobe for steady and visualized detection of albumin in hepatic organoids and mouse liver. *Adv. Sci.* **2022**, *9*, No. 2202505.

(11) Tian, M.; Wang, J.; Li, C.; Wang, Z.; Liu, G.; Lv, E.; Zhao, X.; Li, Z.; Cao, D.; Liu, H.; Zhang, C.; Xu, S.; Man, B. Qualitative and quantitative detection of microcystin-LR based on SERS-FET dual-mode biosensor. *Biosens. Bioelectron.* **2022**, *212*, No. 114434.

(12) Liu, G.; Wang, Z.; Sun, W.; Lin, X.; Wang, R.; Li, C.; Zong, L.; Fu, Z.; Liu, H.; Xu, S. Robust emission in near-infrared II of lanthanide nanoprobes conjugated with Au (LNPs-Au) for temperature sensing and controlled photothermal therapy. *Chem. Eng. J.* **2023**, *452*, No. 139504.

(13) Kitaw, S. L.; Birhan, Y. S.; Tsai, H.-C. Plasmonic surface-enhanced Raman scattering nano-substrates for detection of anionic environmental contaminants: Current progress and future perspectives. *Environ. Res.* **2023**, *221*, No. 115247.

(14) Li, C.; Man, B.; Zhang, C.; Yu, J.; Liu, G.; Tian, M.; Li, Z.; Zhao, X.; Wang, Z.; Cui, W.; Wang, T.; Wang, J.; Lin, X.; Xu, S. Strong plasmon resonance coupling in micro-extraction SERS membrane for in situ detection of molecular aqueous solutions. *Sens. Actuators, B* **2024**, *398*, No. 134767.

(15) McDonnell, C.; Albarghouthi, F.; Selhorst, R.; Kelley-Loughnane, N.; Franklin, A. D.; Rao, R. Aerosol jet printed surface-enhanced Raman substrates: Application for high-sensitivity detection of perfluoroalkyl substances. *ACS Omega* **2023**, *8*, 1597−1605.

(16) Otto, A.; Mrozek, I.; Grabhorn, H.; Akemann, W. Surface-enhanced Raman-scattering. *J. Phys.: Condens. Matter* **1992**, *4*, 1143−1212.

(17) Ding, S. Y.; You, E.; Tian, Z.; Moskovits, M. Electromagnetic theories of surface-enhanced Raman spectroscopy. *Chem. Soc. Rev.* **2017**, *46*, 4042−4076.

(18) Shao, M.; Ji, C.; Tan, J.; Du, B.; Zhao, X.; Yu, J.; Man, B.; Xu, K.; Zhang, C.; Li, Z. Ferroelectrically modulate the Fermi level of graphene oxide to enhance SERS response. *Opto-Electron. Adv.* **2023**, *6*, No. 230094.

(19) Tan, J.; Du, B.; Ji, C.; Shao, M.; Zhao, X.; Yu, J.; Xu, S.; Man, B.; Zhang, C.; Li, Z. Thermoelectric field-assisted Raman scattering and photocatalysis with GaN-plasmonic metal composites. *ACS Photonics* **2023**, *10*, 2216−2225.

(20) Zhang, C.; Tan, J.; Du, B.; Ji, C.; Pei, Z.; Shao, M.; Jiang, S.; Zhao, X.; Yu, J.; Man, B.; Li, Z.; Xu, K. Reversible thermoelectric regulation of electromagnetic and chemical enhancement for rapid SERS detection. *ACS Appl. Mater. Interfaces* **2024**, *16*, 12085−12094.

(21) Aravind, P. K.; Nitzan, A.; Metiu, H. The interaction between electromagnetic resonances and its role in spectroscopic studies of molecules absorbed on colloidal particles or metal spheres. *Surf. Sci.* **1981**, *110*, 189−204.

(22) Duan, H. G.; Fernandez-Dominguez, A. I.; Bosman, M.; Maier, S. A.; Yang, J. K. W. Nanoplasmonics: Classical down to the nanometer scale. *Nano Lett.* **2012**, *12*, 1683−1689.

(23) Coluccio, M. L.; Das, G.; Mecarini, F.; Gentile, F.; Pujia, A.; Bava, L.; Tallerico, R.; Candeloro, P.; Liberale, C.; De Angelis, F.; Di Fabrizio, E. Silver-based surface enhanced Raman scattering (SERS) substrate fabrication using nanolithography and site selective electroless deposition. *Microelectron. Eng.* **2009**, *86*, 1085−1088.

(24) Sivashanmugan, K.; Liao, J.; Yao, C. Nanovoids embedded in FIB-fabricated Au/Ag nanorod arrays for ultrasensitive SERS-active substrate. *Appl. Phys. Express* **2014**, *7*, No. 092202.
(25) Virga, A.; Rivolo, P.; Frascella, F.; Angelini, A.; Descrovi, E.; Geobaldo, F.; Giorgis, F. Silver nanoparticles on porous silicon: approaching single molecule detection in resonant SERS regime. *J. Phys. Chem. C* **2013**, *117*, 20139−20145.
(26) Lee, W.; Lee, S. Y.; Briber, R. M.; Rabin, O. Self-Assembled SERS substrates with tunable surface plasmon resonances. *Adv. Funct. Mater.* **2011**, *21*, 3424−3429.
(27) Guo, S.; Dong, S. Metal nanomaterial-based self-assembly: Development, electrochemical sensing and SERS applications. *J. Mater. Chem.* **2011**, *21*, 16704−16716.
(28) Dzhagan, V.; Mazur, N.; Kapush, O.; Skoryk, M.; Pirko, Y.; Yemets, A.; Dzhahan, V.; Shepeliavyi, P.; Valakh, M.; Yukhymchuk, V. Self-organized SERS substrates with efficient analyte enrichment in the hot spots. *ACS Omega* **2024**, *9*, 4819−4830.
(29) Mazur, N. V.; Kapush, O. A.; Isaieva, O. F.; Budzulyak, S. I.; Buziashvili, A. Y.; Pirko, Y. V.; Skoryk, M. A.; Yemets, A. I.; Hreshchuk, O. M.; Yukhymchuk, V. O.; Dzhagan, V. M. Facile SERS substrates from Ag nanostructures chemically synthesized on glass surfaces. *Phys. Chem. Solid State* **2023**, *24*, 682−691.
(30) Chakraborti, S.; Basu, R. N.; Panda, S. K. Vertically aligned silicon nanowire array decorated by Ag or Au nanoparticles as SERS substrate for bio-molecular detection. *Plasmonics* **2018**, *13*, 1057−1080.
(31) Yin, Z.; Ni, C.; Wu, S. Femtosecond laser direct writing processing of SERS substrates and applications. *Opto-Electron. Eng.* **2023**, *50*, No. 220322.
(32) Wang, H.; Liu, S.; Zhang, Y.; Wang, J.; Wang, L.; Xia, H.; Chen, Q.; Ding, H.; Sun, H. Controllable assembly of silver nanoparticles induced by femtosecond laser direct writing. *Sci. Technol. Adv. Mater.* **2015**, *16*, No. 024805.
(33) Cheng, C.-W.; Chang, C.; Chen, J.; Wang, B. Femtosecond laser melting of silver nanoparticles: comparison of model simulations and experimental results. *Appl. Phys. A: Mater. Sci. Process.* **2018**, *124*, No. 371.
(34) Liang, J.; Wang, X.; Zhou, X.; Kang, H.; Peng, P. Joining process of copper nanoparticles with femtosecond laser irradiation. *Chin. J. Lasers* **2021**, *48*, No. 0802008.
(35) Wang, Q.; Zhang, R.; Chen, Q.; Duan, R. A review of femtosecond laser processing of silicon carbide. *Micromachines* **2024**, *15*, 639.
(36) Zhang, X.; Zhang, X.; Luo, C.; Liu, Z.; Chen, Y.; Dong, S.; Jiang, C.; Yang, S.; Wang, F.; Xiao, X. Volume-enhanced Raman scattering detection of viruses. *Small* **2019**, *15*, No. 1805516.
(37) Tian, Y.; Wang, H.; Yan, L.; Zhang, X.; Falak, A.; Guo, Y.; Chen, P.; Dong, F.; Sun, L.; Chu, W. A generalized methodology of designing 3D SERS probes with superior detection limit and uniformity by maximizing multiple coupling effects. *Adv. Sci.* **2019**, *6*, No. 1900177.
(38) Li, S.; Zhang, N.; Zhang, N.; Lin, D.; Hu, X.; Yang, X. Three-dimensional ordered Ag/ZnO/Si hierarchical nanoflower arrays for spatially uniform and ultrasensitive SERS detection. *Sens. Actuators, B* **2020**, *321*, No. 128519.
(39) Meng, L.; Shang, L.; Feng, S.; Tang, Z.; Bi, C.; Zhao, H.; Liu, G. Fabrication of a three-dimensional (3D) SERS fiber probe and application of in situ detection. *Opt. Express* **2022**, *30*, 2353−2363.
(40) Zhang, X.; Liu, H.; Feng, S. Solution-processible fabrication of large-area patterned and unpatterned gold nanostructures. *Nanotechnology* **2009**, *20*, No. 425303.
(41) Tayama, M.; Inose, T.; Yamauchi, N.; Nakashima, K.; Tokunaga, M.; Kato, C.; Gonda, K.; Kobayashi, Y. Fabrication of gold-immobilized quantum dots/silica core-shell nanoparticles and their multimodal imaging properties. *Part. Sci. Technol.* **2022**, *40*, 252−260.
(42) Liu, H.; Zhang, X.; Zhai, T.; Sander, T.; Chen, L.; Klar, P. J. Centimeter-scale-homogeneous SERS substrates with seven-order global enhancement through thermally controlled plasmonic nanostructures. *Nanoscale* **2014**, *6*, 5099−5105.
(43) Cao, B.; Mu, Y.; Zhang, X. Direct laser annealing of surface-enhanced Raman scattering substrates. *Adv. Eng. Mater.* **2019**, *21*, No. 1900779.
(44) Hostetler, M. J.; Wingate, J. E.; Zhong, C. J.; Harris, J. E.; Vachet, R. W.; Clark, M. R.; Londono, J. D.; Green, S. J.; Stokes, J. J.; Wignall, G. D.; Glish, G. L.; Porter, M. D.; Evans, N. D.; Murray, R. W. Alkanethiolate gold cluster molecules with core diameters from 1.5 to 5.2 nm: Core and monolayer properties as a function of core size. *Langmuir* **1998**, *14*, 17−30.
(45) Chang, Y.-C.; Lu, Y.; Hung, Y. Controlling the nanoscale gaps on silver island film for efficient surface-enhanced Raman spectroscopy. *Nanomaterials* **2019**, *9*, 470.
(46) Yukhymchuk, V. O.; Kostyukevych, S. A.; Dzhagan, V. M.; Milekhin, A. G.; Rodyakina, E. E.; Yanchuk, I. B.; Shepeliavy, P. Y.; Valakh, M.Y.; Kostyukevych, K. V.; Lysiuk, V. O.; Tverdokhlib, I. V. SERS of Rhodamine 6G on substrates with laterally ordered and random gold nanoislands. *Semicond. Phys., Quantum Electron. Optoelectron.* **2012**, *15*, 232−238.
(47) Gaspar, D.; Pimentel, A. C.; Mateus, T.; Leitao, J. P.; Soares, J.; Falcao, B. P.; Araújo, A.; Vicente, A.; Filonovich, S. A.; Aguas, H.; Martins, R.; Ferreira, I. Influence of the layer thickness in plasmonic gold nanoparticles produced by thermal evaporation. *Sci. Rep.* **2013**, *3*, No. 1469.
(48) Hreshchuk, O. M.; Yukhymchuk, V. O.; et al. Efficient SERS substrates based on laterally ordered gold nanostructures made using interference lithography. *Semicond. Phys., Quantum Electron. Optoelectron.* **2019**, *22*, 215−223.
(49) Brognara, A.; Nasri, I. F. M. A.; Bricchi, B. R.; Li Bassi, A.; Gauchotte-Lindsay, C.; Ghidelli, M.; Lidgi-Guigui, N. Highly sensitive detection of estradiol by a SERS sensor based on TiO_2 covered with gold nanoparticles. *Beilstein J. Nanotechnol.* **2020**, *11*, 1026−1035.
(50) Le Ru, E. C.; Blackie, E.; Meyer, M.; Etchegoin, P. G. Surface-enhanced Raman scattering enhancement factors: A comprehensive study. *J. Phys. Chem. C* **2007**, *111*, 13794−13803.
(51) Dinish, U. S.; Yaw, F. C.; Agarwal, A.; Olivo, M. Development of highly reproducible nanogap SERS substrates: Comparative performance analysis and its application for glucose sensing. *Biosens. Bioelectron.* **2011**, *26*, 1987−1992.

https://doi.org/10.1021/acsomega.4c04588
ACS Omega 2024, 9, 37188−37196